



Spectroscopic Validation of Low-metallicity Stars from RAVE

Vinicius M. Placco^{1,2,18}, Timothy C. Beers^{1,2}, Rafael M. Santucci^{3,4}, Julio Chaname^{5,6}, María Paz Sepúlveda^{5,6}, Johanna Coronado^{5,7}, Sean D. Points⁸, Catherine C. Kaleida⁹, Silvia Rossi¹⁰, Georges Kordopatis¹¹, Young Sun Lee¹², Gal Matijević¹³, Anna Frebel^{2,14}, Terese T. Hansen¹⁵, Erika M. Holmbeck^{1,2}, Kaitlin C. Rasmussen^{1,2}, Ian U. Roederer^{2,16}, Charli M. Sakari¹⁷, and Devin D. Whitten^{1,2}

¹ Department of Physics, University of Notre Dame, Notre Dame, IN 46556, USA; vplacco@nd.edu

² Joint Institute for Nuclear Astrophysics, Center for the Evolution of the Elements, 1 Cyclotron Laboratory, National Superconducting Cyclotron Laboratory, Michigan State University, East Lansing, MI 48824-1321, USA

³ Instituto de Estudos Sócio-Ambientais, Planetário, Universidade Federal de Goiás, Goiânia, GO 74055-140, Brazil

⁴ Instituto de Física, Universidade Federal de Goiás, Campus Samambaia, Goiânia, GO 74001-970, Brazil

⁵ Instituto de Astrofísica, Pontificia Universidad Católica de Chile, Santiago, Chile

⁶ Millennium Institute of Astrophysics, Santiago, Chile

⁷ Max-Planck-Institut für Astronomie, Königstuhl 17, D-69117 Heidelberg, Germany

⁸ Cerro Tololo Inter-American Observatory, Casilla 603, La Serena, Chile

⁹ Space Telescope Science Institute, Baltimore, MD 21218, USA

¹⁰ Instituto de Astronomia, Geofísica e Ciências Atmosféricas, Universidade de São Paulo, SP 05508-900, Brazil

¹¹ Laboratoire Lagrange, Université Côte d'Azur, Observatoire de la Côte d'Azur, CNRS, F-06304 Nice cedex 4, France

¹² Department of Astronomy and Space Science, Chungnam National University, Daejeon 34134, Republic of Korea

¹³ Leibniz Institut für Astrophysik Potsdam (AIP), An der Sternwarte 16, D-14482 Potsdam, Germany

¹⁴ Department of Physics and Kavli Institute for Astrophysics and Space Research, Massachusetts Institute of Technology, Cambridge, MA 02139, USA

¹⁵ Observatories of the Carnegie Institution of Washington, Pasadena, CA 91101, USA

¹⁶ Department of Astronomy, University of Michigan, Ann Arbor, MI 48109, USA

¹⁷ Department of Astronomy, University of Washington, Seattle, WA 98195-1580, USA

Received 2018 March 14; revised 2018 April 27; accepted 2018 April 30; published 2018 May 31

Abstract

We present results from a medium-resolution ($R \sim 2000$) spectroscopic follow-up campaign of 1694 bright ($V < 13.5$), very metal-poor star candidates from the RAdial Velocity Experiment (RAVE). Initial selection of the low-metallicity targets was based on the stellar parameters published in RAVE Data Releases 4 and 5. Follow up was accomplished with the Gemini-N and Gemini-S, the ESO/NTT, the KPNO/Mayall, and the SOAR telescopes. The wavelength coverage for most of the observed spectra allows for the determination of carbon and α -element abundances, which are crucial for considering the nature and frequency of the carbon-enhanced metal-poor (CEMP) stars in this sample. We find that 88% of the observed stars have $[\text{Fe}/\text{H}] \leq -1.0$, 61% have $[\text{Fe}/\text{H}] \leq -2.0$, and 3% have $[\text{Fe}/\text{H}] \leq -3.0$ (with four stars at $[\text{Fe}/\text{H}] \leq -3.5$). There are 306 CEMP star candidates in this sample, and we identify 169 CEMP Group I, 131 CEMP Group II, and 6 CEMP Group III stars from the $A(C)$ versus $[\text{Fe}/\text{H}]$ diagram. Inspection of the $[\alpha/\text{C}]$ abundance ratios reveals that five of the CEMP Group II stars can be classified as “mono-enriched second-generation” stars. *Gaia* DR1 matches were found for 734 stars, and we show that transverse velocities can be used as a confirmatory selection criteria for low-metallicity candidates. Selected stars from our validated list are being followed-up with high-resolution spectroscopy to reveal their full chemical-abundance patterns for further studies.

Key words: Galaxy: halo – stars: abundances – stars: atmospheres – stars: carbon – stars: Population II – techniques: imaging spectroscopy

Supporting material: machine-readable tables

1. Introduction

Low-metallicity stars provide a direct window on the origin of the first (Population III) stars to form in the universe and on the chemical and dynamical evolution of the Milky Way (Beers & Christlieb 2005; Frebel & Norris 2015; Chiaki et al. 2017; Jeon et al. 2017). In particular, as sample sizes have grown over the last few decades, interest has focused on the nature of the very metal-poor (VMP; $[\text{Fe}/\text{H}]^{19} < -2.0$), extremely metal-poor (EMP; $[\text{Fe}/\text{H}] < -3.0$), and ultra metal-poor (UMP; $[\text{Fe}/\text{H}] < -4.0$) stars. Detailed spectroscopic studies of these objects are the best way to identify and distinguish between a number of possible scenarios for the enrichment of early star-

forming gas clouds soon after the Big Bang (see, e.g., Norris et al. 2013; Yong et al. 2013; Hansen et al. 2014; Placco et al. 2014b, 2015b, 2016b; Roederer et al. 2014b; Frebel et al. 2015; Hansen et al. 2015).

Furthermore, it has been recognized that carbon is ubiquitous in the early universe, based on empirical evidence that the frequencies of carbon-enhanced metal-poor (CEMP; $[\text{C}/\text{Fe}] \geq +0.7$, e.g., Beers & Christlieb 2005; Aoki et al. 2007) stars increase with decreasing stellar metallicity, from 20% for VMP stars to at least 80% for UMP stars (Placco et al. 2014c). The full elemental-abundance patterns for CEMP stars are required in order to probe the nature of the different progenitor populations responsible for the production of carbon and other elements. Recent studies (e.g., Yoon et al. 2016 and references therein) show that the majority of CEMP stars with $[\text{Fe}/\text{H}] \leq -3.0$ belong to the CEMP-no subclass, characterized

¹⁸ Visiting astronomer, Kitt Peak National Observatory.

¹⁹ $[A/B] = \log(N_A/N_B)_* - \log(N_A/N_B)_\odot$, where N is the number density of atoms of a given element in the star ($*$) and the Sun (\odot), respectively.

Table 1
Observing Details

Star Name (RAVE)	Date (UTC)	Telescope	Instrument	Proposal ID	Exp. (s)
J000022.6–130228	2014 Sep 11	Mayall	RCSPEC	14B-0231	720
J000024.2–110746	2014 Sep 12	Mayall	RCSPEC	14B-0231	600
J000245.9–325734	2015 Aug 21	Gemini-S	GMOS-S	GS-2015A-Q-205	720
J000351.1–123154	2014 Sep 12	Mayall	RCSPEC	14B-0231	720
J000414.3–265709	2014 Oct 29	SOAR	Goodman	2014B-0231	30

(This table is available in its entirety in machine-readable form.)

Table 2
Coordinates, Magnitudes, Color Indices, and Reddening Estimates

Star Name (RAVE)	α (J2000)	δ (J2000)	l (deg)	b (deg)	V (mag)	$(B - V)$	J (mag)	$(J - K)$	$E(B - V)$
J000022.6–130228	00:00:22.59	–13:02:27.5	80.127	–71.531	12.891	0.904	11.020	0.610	0.024
J000024.2–110746	00:00:24.16	–11:07:45.5	83.613	–70.002	12.023	0.912	10.254	0.633	0.030
J000245.9–325734	00:02:45.90	–32:57:34.3	1.006	–77.973	12.030	0.681	10.584	0.509	0.011
J000351.1–123154	00:03:51.14	–12:31:53.9	83.240	–71.634	12.878	0.777	11.252	0.572	0.026
J000414.3–265709	00:04:14.29	–26:57:08.6	31.197	–79.492	10.801	0.975	8.941	0.665	0.013

(This table is available in its entirety in machine-readable form.)

by a lack of enhancements in the neutron-capture elements (e.g., $[\text{Ba}/\text{Fe}] < 0.0$). The brightest EMP star in the sky, BD +44:493, with $[\text{Fe}/\text{H}] = -3.8$ and $V = 9.0$, is a CEMP-no star (Ito et al. 2013; Placco et al. 2014a) and shares a common light-element abundance signature with the most iron-poor star observed to date ($[\text{Fe}/\text{H}] \leq -7.5$; Keller et al. 2014; Bessell et al. 2015). The distinctive CEMP-no pattern has also been identified in high- z damped Ly α systems (Cooke et al. 2012; Cooke & Madau 2014) and is common among stars in the ultra-faint dwarf spheroidal galaxies, such as Segue-1 (Frebel et al. 2014). These, and other observations, suggest that CEMP-no stars exhibit the nucleosynthesis products of the first generation of stars (Sharma et al. 2017; Hartwig et al. 2018).

Another important subclass of metal-poor stars are the objects that exhibit over-abundances in elements synthesized by the rapid neutron-capture process (r -process; Burbidge et al. 1957; Cameron 1957). The so-called r -II stars are identified by enhancements in europium ($[\text{Eu}/\text{Fe}] \geq +1.0$) and a low Ba abundance relative to Eu ($[\text{Ba}/\text{Eu}] \leq 0.0$; Beers & Christlieb 2005). These stars are believed to be formed preferentially in ultra-faint dwarf galaxies (Ji et al. 2016; Roederer et al. 2016a), and their abundance patterns have been suggested to arise from the nucleosynthesis products of a neutron star merger (Lattimer & Schramm 1974). Recent photometric and spectroscopic observations of the electromagnetic counterpart of the gravitational wave event GW170817 has confirmed this association (Abbott et al. 2017; Drout et al. 2017; Shappee et al. 2017).

The first r -II star, CS-22892-052, was identified by Sneden et al. (1994), based on high-resolution spectroscopic follow up of VMP/EMP stars discovered in the HK survey (Beers et al. 1985, 1992). Over time, the numbers of known r -II stars slowly grew. Dedicated observational efforts, beginning with the work of Christlieb et al. (2004) and Barklem et al. (2005), and more recently, by Roederer et al. (2014a), and others (typically one or two stars at a time), have been able to identify a total of ~ 25 – 30 r -II stars, which account for roughly 3% of the population of VMP stars. Most recently, the R -Process

Alliance (RPA) was established (e.g., Hansen et al. 2018), with the aim to at least quadruple the number of known r -II stars over the next few years, and to study their abundance patterns at high spectral resolution.

Over the last 25 years, large-scale survey efforts have dramatically increased the numbers of known low-metallicity stars in the Galaxy, enabling their further study with high-resolution spectroscopy. Together, the HK survey (Beers et al. 1985, 1992) and the Hamburg/ESO Survey (HES; Frebel et al. 2006; Christlieb et al. 2008) identified several thousand VMP stars. To date, two of the three most metal-poor stars found in the halo of the Galaxy, HE 0107–5240 ($[\text{Fe}/\text{H}] = -5.2$; Christlieb et al. 2002) and HE 1327–2326 ($[\text{Fe}/\text{H}] = -5.6$; Frebel et al. 2005), were first identified from spectroscopic follow up of candidates in the HES database. These numbers have been further increased through the use of medium-resolution spectroscopy carried out during the SDSS (York et al. 2000) and the sub-surveys Sloan Extension for Galactic Understanding and Exploration (SEGUE-1; Yanny et al. 2009) and SEGUE-2, to many tens of thousands of VMP (and ~ 1000 EMP) stars.

However, due to limitations in the input source catalogs (e.g., saturation of the HK/HES prism plates, and the $g \sim 14$ bright limit from SDSS scans), the above surveys have not been able to provide large numbers of VMP/EMP stars with $V < 12$. Yet, bright examples of such stars are the *best available targets* for high-resolution spectroscopic follow up, as they can be readily observed to very high S/N with 4m- and 8m-class ground-based telescopes, and are the *only stars* that can be observed at high spectral resolution in the near-UV with the *Hubble Space Telescope* (e.g., Sneden et al. 1998; Roederer 2012; Roederer et al. 2012, 2014c, 2016b; Placco et al. 2014a, 2015a).

The RAdial Velocity Experiment (RAVE; Steinmetz et al. 2006) survey has broken through this limitation and has determined atmospheric parameters and accurate radial velocities for a magnitude-limited ($9 < I < 12$) sample of over 400,000 stars in the southern hemisphere (DR4; Kordopatis

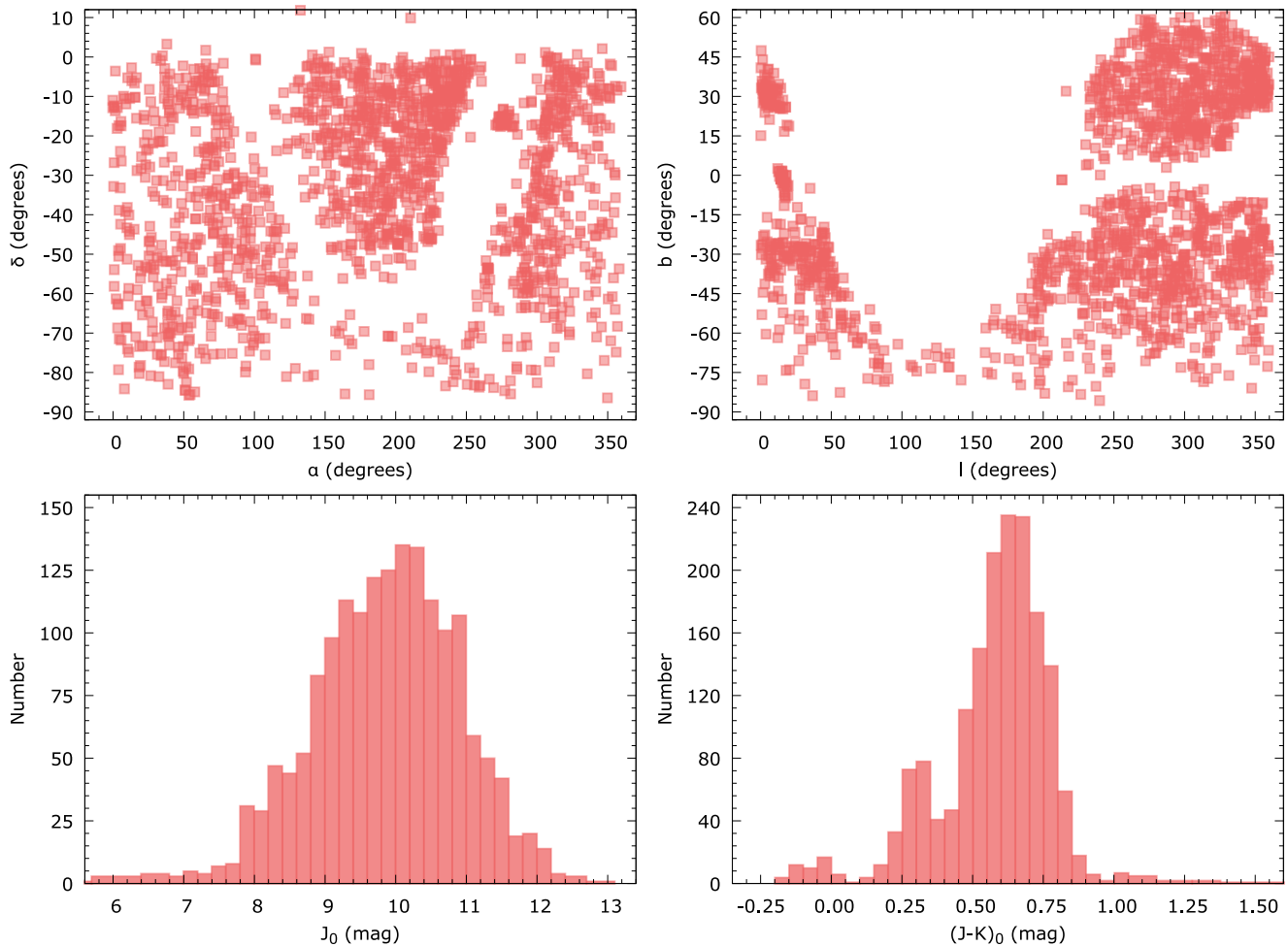


Figure 1. Upper panels: equatorial and Galactic coordinates for the observed targets. Lower panels: distributions of absorption-corrected J_0 magnitudes and de-reddened $(J - K)_0$ colors.

et al. 2013), based on moderate-resolution spectroscopy ($R \sim 8000$). Even though RAVE provides reasonably reliable atmospheric-parameter estimates (T_{eff} , $\log g$, and $[\text{Fe}/\text{H}]$), it is not possible for RAVE to measure $[\text{C}/\text{Fe}]$, as prominent carbon-related features lie outside their narrow spectral region, centered on the Ca I triplet at $\sim 8500 \text{ \AA}$.²⁰

In this paper, we report on the medium-resolution ($R \sim 2000$) spectroscopic follow up of VMP star candidates selected from RAVE. The main goals are to determine carbon abundances for a large sample of metal-poor stars from RAVE and to validate the published RAVE atmospheric-parameter estimates. Once identified, interesting targets are re-observed with high-resolution spectroscopy, in order to determine their full chemical-abundance patterns. This paper is outlined as follows. Section 2 describes the target selection for the medium-resolution spectroscopic investigation and the follow-up observations, followed by the determinations of the stellar atmospheric parameters and abundances in Section 3. We provide a comparison between the RAVE parameters and our determinations in Section 4, and present *Gaia* DR1-based distances and proper motions for a subset of our targets in

²⁰ Other ongoing surveys, including the Best & Brightest survey of Schlafman & Casey (2014) and the SkyMapper survey (Keller et al. 2007), have also identified large numbers of bright VMP candidate stars. Medium- and high-resolution spectroscopy of stars from these surveys have been collected as part of the RPA effort, and will be reported on in due course.

Section 5. Section 6 describes the importance of the carbon and α -element abundances in further selecting targets for high-resolution follow up. Our concluding remarks are provided in Section 7.

2. Target Selection and Observations

The final data release of the RAVE (DR5; Kunder et al. 2017) presents atmospheric parameters, radial velocities, individual abundances, and distances for 520,701 stars, mostly in the $9 < I < 12$ magnitude range. Due to its limited spectral range (8410–8795 \AA), it is not possible to determine carbon abundances for these stars based on RAVE spectra alone. There are several advantages in working with RAVE DR5 data: (i) their relatively reliable $[\text{Fe}/\text{H}]$ estimates help in selecting only metal-poor candidates and avoid color-dependent effects that can compromise this kind of selection, and (ii) the radial velocities of the RAVE stars have an average error of no more than a few km s^{-1} . These velocities, together with reliable proper motions and parallaxes from the *Gaia* mission, will allow for precision determinations of the full space motions that are required for further kinematic analysis.

2.1. Target Selection from the RAVE Database

RAVE presents the ideal sample for our proposed search for bright low-metallicity stars with medium-resolution

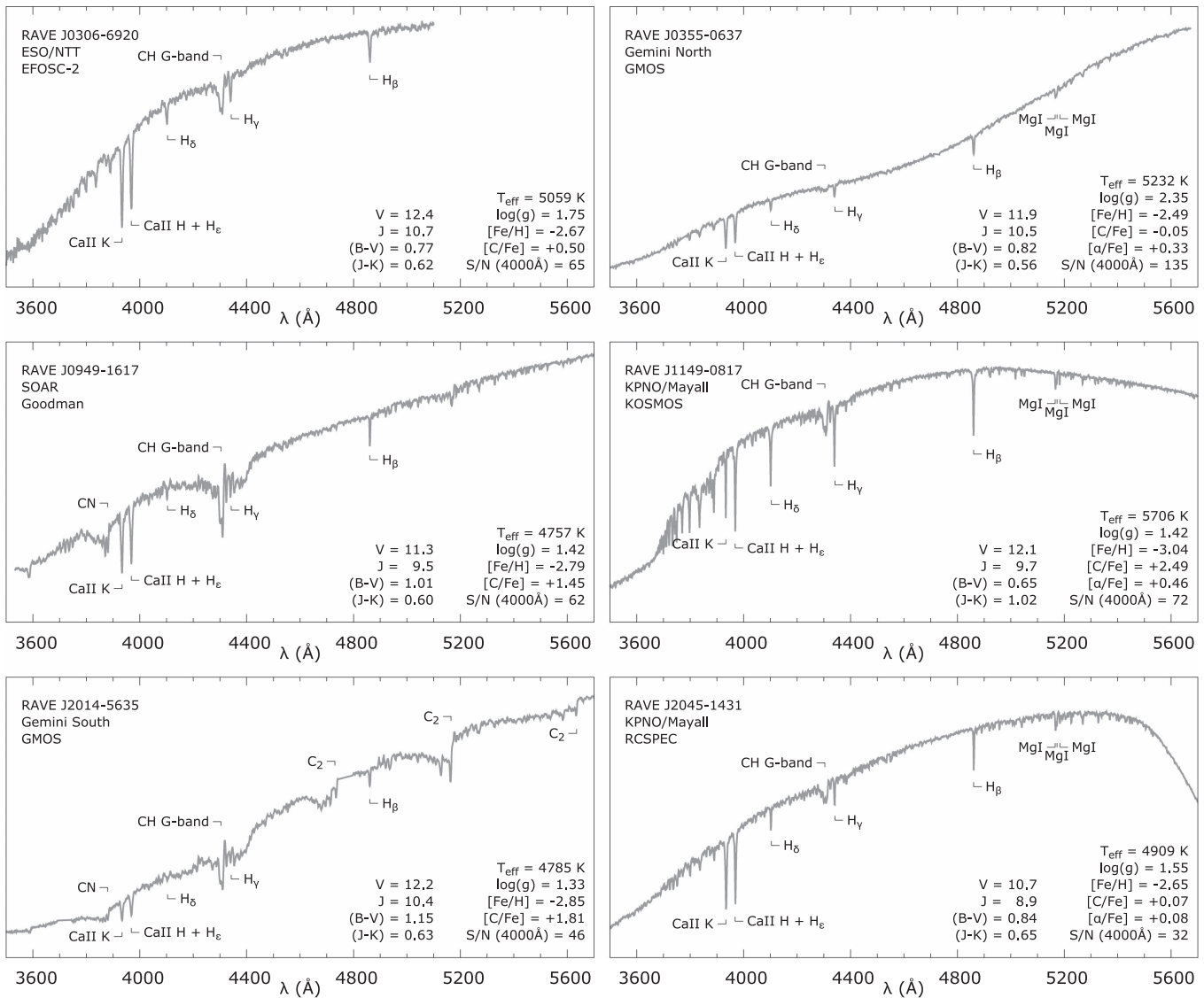


Figure 2. Example medium-resolution spectra for six RAVE stars observed with the resources described in Section 2.2. The magnitudes, colors, and estimated parameters are listed in the lower-right part of each panel (see details in Section 3). Prominent absorption features are identified in each spectrum.

spectroscopy. Since RAVE provides stellar parameters, we could be quite selective on the temperatures and metallicities of each target before carrying out our spectroscopic follow up, roughly covering the wavelength range [3500:5500] \AA .

There are three primary goals: (i) Obtain $[C/Fe]$ and $[\alpha/Fe]$ estimates for a large number of metal-poor stars in RAVE, (ii) Derive estimates of the fractions of CEMP stars, as a function of $[Fe/H]$, for a large unbiased sample of halo stars, selected without a priori knowledge of the likelihood of carbon enhancement, and (iii) Determine, on the basis of the full space motions of these stars (when available), the fractions of CEMP stars associated with the inner- and outer-halo populations of the Galaxy.

The low-metallicity candidates were selected from the RAVE DR4 and DR5 catalogs. The selection criteria were applied to the RAVE stellar parameters ($3500 < T_{\text{eff}}(\text{K})^{21} < 7000$; $[Fe/H]^{22} \leq -1.5$) and 2MASS photometric quality flags ($ph_qual_{JHK} = \text{AAA}$; Skrutskie

et al. 2006). We also tracked (but did not use for the selection) the internal quality flag from the RAVE stellar parameter pipeline (QK-`Algo_Conv_K`), the signal-to-noise ratio (S/N) for two different pipeline implementations (`STN_SPARV` and `SNR_K`), and the first three morphological flags (`c1/c2/c3`; Matijevič et al. 2012) for each star. These were used to assess possible discrepancies between the RAVE parameters and the values determined by our spectroscopic follow up (see Section 4 for further details). That is, we sought to explore which of the RAVE flags should be used to exclude potential contaminating stars in our search and which could be ignored.

2.2. Medium-resolution Follow-up Observations

The medium-resolution spectroscopic follow-up campaign was conducted from semesters 2014A to 2017A and collected 1835 spectra of 1694 unique metal-poor candidates. We used six different telescope/instrument setups: (i) SOAR/Goodman, (ii) Gemini North/GMOS-N, (iii) Gemini South/GMOS-S, (iv) Mayall/RCSPEC, (v) Mayall/KOSMOS, and (vi) NTT/EFOSC-2. Table 1 lists the object name, observation date,

²¹ $T_{\text{eff_K}}$ for DR4 and $T_{\text{eff_N_K}}$ for DR5.

²² $c[M/H]_{\text{K}}$ for DR4 and $Met_{\text{N_K}}$ for DR5.

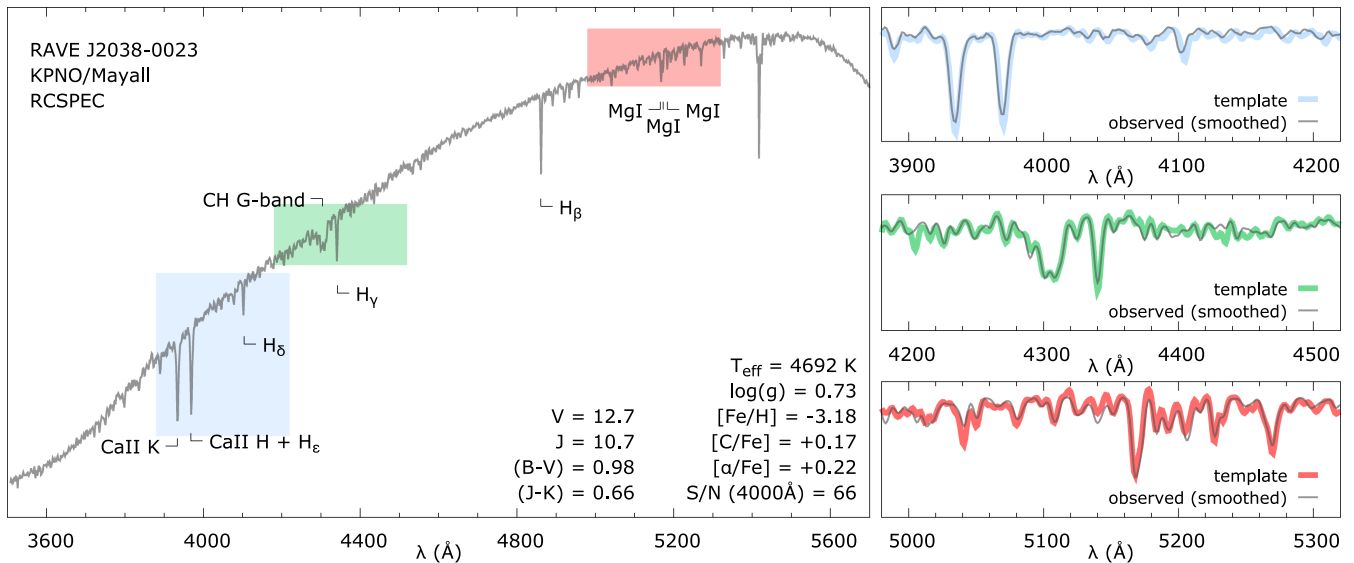


Figure 3. Left panel: example RCSPEC spectrum in the wavelength range as analyzed by the n-SSPP, with key absorption features identified. Right panels: comparison between the observed and the synthetic spectra, generated using the parameters listed on the left panel. The Ca II K line (top right) is used to determine $[Fe/H]$; $[C/Fe]$ is determined from the CH G-band (middle right); and the Mg I triplet (lower right) is used to estimate $[\alpha/Fe]$.

telescope, instrument, program ID, and exposure time for the observed candidates. Table 2 lists their coordinates, magnitudes, color indices, and reddening estimates (Schlegel et al. 1998). Figure 1 shows the equatorial and Galactic coordinates of the observed targets, as well as the distribution of their extinction-corrected J_0 magnitudes and de-reddened $(J - K)_0$ color indices.

Details on each observing setup are provided below. For consistency across the different instruments, we chose grating/slit combinations that would yield a resolving power $R \sim 1200$ – 2000 , and exposure times sufficient to reach an S/N of at least ~ 40 per pixel at the Ca II K line (3933.3 \AA). The average value for the 1694 observed spectra is $S/N \sim 54$ at 4000 \AA . Calibration frames included arc-lamp exposures, bias frames, and quartz flats. All tasks related to spectral reduction, extraction, and wavelength calibration were performed using standard IRAF²³ packages (see Placco et al. 2013, for further details).

SOAR Telescope—335 stars were observed with the 4.1 m Southern Astrophysical Research (SOAR) telescope. The Goodman Spectrograph was used with the 600 l mm^{-1} grating, the blue setting, and a $1''.03$ slit, resulting in a wavelength coverage in the range $[3600:6200] \text{ \AA}$ at resolving power $R \sim 1500$. An example Goodman spectrum can be seen on the middle-left panel of Figure 2.

Gemini North and South Telescopes—192 stars were observed with the twin 8.1 m Gemini North (30 stars) and Gemini South (162 stars) telescopes. In both cases, we used the 600 l mm^{-1} grating (G5323 for GMOS South and G5307 for GMOS North) and a $1''.00$ slit, resulting in a wavelength coverage in the range $[3200:5800] \text{ \AA}$ at resolving power $R \sim 2000$. Example GMOS-N and GMOS-S spectra can be seen in the top-right and bottom-left panels of Figure 2, respectively.

KPNO Mayall Telescope—444 stars were observed with the 4 m Mayall telescope, located at Kitt Peak National Observatory, using the R-C spectrograph (337 stars) and the KOSMOS

spectrograph (107 stars). For the R-C spectrograph, we used the KPC007 grating (632 l mm^{-1}), the blue setting, and a $1''.0$ slit, resulting in a wavelength coverage in the range $[3500:6000] \text{ \AA}$ at resolving power $R \sim 1500$. For the KOSMOS spectrograph, we used the 600 l mm^{-1} grating, the blue setting, and a $0''.9$ slit, resulting in a wavelength coverage in the range $[3600:6300] \text{ \AA}$ at resolving power $R \sim 1800$. Example RCSPEC and KOSMOS spectra can be seen in the bottom-right and middle-right panels of Figure 2, respectively.

ESO New Technology Telescope (NTT)—723 stars were observed with the 3.58 m NTT, located at La Silla Observatory, part of the European Southern Observatory. We used the EFOSC-2 spectrograph with Grism#7 (600 gr mm^{-1}) and a $1''.0$ slit, resulting in a wavelength coverage in the range $[3300:5100] \text{ \AA}$ at resolving power $R \sim 1200$. An example EFOSC-2 spectrum can be seen in the top-left panel of Figure 2.

3. Stellar Parameters and Abundances

The stellar atmospheric parameters, as well as carbon and α -element abundances, were determined using the n-SSPP (Beers et al. 2014, 2017), a modified version of the SEGUE Stellar Parameter Pipeline (SSPP; Lee et al. 2008a, 2008b, 2013). Figure 3 shows an example processing of the n-SSPP for the spectrum of RAVE J2038–0023,²⁴ observed with RCSPEC on KPNO/Mayall. The left panel shows the entire wavelength range, and identifies key absorption features used for parameter estimation. The right panels show comparisons between the observed spectrum and the synthetic spectrum generated by the n-SSPP using the parameters quoted on the left panel (i.e., the synthetic spectrum is not a fit, but a prediction). The Ca II K line (top right) is used to determine $[Fe/H]$; $[C/Fe]$ is determined from the CH G-band (middle right); and the Mg I triplet (lower right) is used to estimate $[\alpha/Fe]$.

²⁴ The parameters determined from the n-SSPP for this star motivated us to obtain high-resolution spectroscopic follow up using MIKE/Magellan. RAVE J2038–0023 was then identified as the first r -process-enhanced star identified in the RAVE database (Placco et al. 2017).

²³ <http://iraf.noao.edu>

Table 3
Stellar Parameters from RAVE DR4, RAVE DR5, RAVE-on, and the n-SSPP

Star Name (RAVE)	RAVE DR4				RAVE DR5					RAVE-on				This work					
	V_r (km s ⁻¹)	T_{eff} (K)	log g (cgs)	[Fe/H]	V_r (km s ⁻¹)	T_{eff} (K)	T_{effIR} (K)	log g (cgs)	[Fe/H]	V_r (km s ⁻¹)	T_{eff} (K)	log g (cgs)	[Fe/H]	T_{eff} (K)	log g (cgs)	[Fe/H]	[C/Fe]	Δ [C/Fe]	[α /Fe]
J000022.6–130228	-92.56	4704	1.05	-2.86	-92.56	4687	4797	1.51	-2.60	-92.56	6155	4.13	-1.55	4874	1.45	-2.94	+0.18	+0.45	+0.03
J000024.2–110746	-109.94	4836	4887	2.29	-2.10	-109.94	4879	1.11	-2.08	4772	1.24	-2.47	-0.09	+0.62	+0.15
J000245.9–325734	23.25	4745	0.78	-2.24	23.25	4714	5281	1.26	-2.10	23.25	5022	1.70	-1.95	5312	2.79	-1.88	+0.37	+0.01	+0.12
J000351.1–123154	44.99	4955	1.84	-1.92	44.99	4951	5067	2.23	-1.90	44.99	5490	3.38	-1.54	5128	2.70	-2.14	+0.28	+0.01	+0.21
J000414.3–265709	-46.12	4545	0.19	-2.01	-46.12	4506	4748	0.70	-1.90	-45.46	4766	1.26	-1.52	4877	1.58	-1.81	-0.16	+0.36	+0.27

(This table is available in its entirety in machine-readable form.)

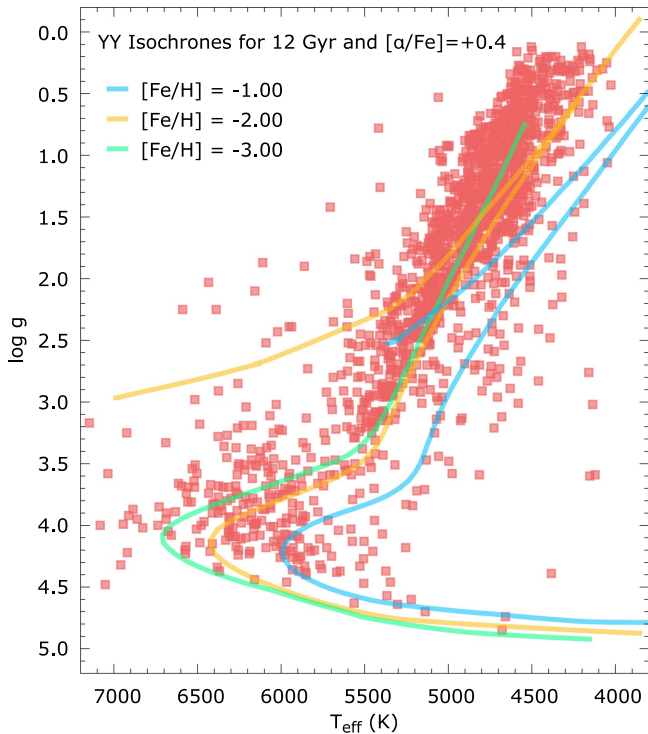


Figure 4. H–R diagram for the program stars, using the parameters calculated by the n-SSPP, listed in Table 3. Overplotted are the YY Isochrones (12 Gy, $0.8 M_{\odot}$, $[\alpha/\text{Fe}] = +0.4$; Demarque et al. 2004) for $[\text{Fe}/\text{H}] = -2.0$, -2.5 , and -3.0 , and horizontal-branch tracks from Dotter et al. (2008).

Atmospheric parameters were determined for $\sim 95\%$ of the observed sample (1614 out of 1694 stars). The nondeterminations arise from a lack of temperature estimates by the n-SSPP, due mostly to stars outside the $[4000:7000] T_{\text{eff}}$ range or stars with core emission in the Ca II K line. The $[\text{C}/\text{Fe}]$ and $[\alpha/\text{Fe}]$ abundance ratios were calculated for 1606 and 849 stars, respectively. The carbon-abundance determination is not carried out for spectra with $\text{S/N} < 10$ and/or when high temperature renders the CH G -band molecular feature too weak to be useful (e.g., Placco et al. 2016a). In addition, $[\alpha/\text{Fe}]$ could not be calculated for the NTT/EFOSC-2 spectra, due to the lack of spectral coverage. The final parameters and abundances for the sample are listed in Table 3, as well as radial velocities and atmospheric parameters from RAVE DR4 and DR5.

From the 1614 stars with estimated metallicities, 1413 (88%) have $[\text{Fe}/\text{H}] \leq -1.0$, 980 (61%) have $[\text{Fe}/\text{H}] \leq -2.0$, and 53 (3%) of the observed stars have $[\text{Fe}/\text{H}] \leq -3.0$. The distribution of effective temperatures and surface gravities derived for the RAVE follow-up sample are shown in Figure 4, compared with Yale-Yonsei Isochrones (12 Gy, $0.8 M_{\odot}$, $[\alpha/\text{Fe}] = +0.4$; Demarque et al. 2004) for $[\text{Fe}/\text{H}] = -2.0$, -2.5 , and -3.0 . Also shown are the Horizontal-Branch tracks from the Dartmouth Stellar Evolution Database (Dotter et al. 2008), using the same input parameters. As RAVE is a magnitude-limited survey, it is expected that our sample would be dominated by sub-giants and giants. We also include corrections for the carbon abundances, based on the stellar-evolution models presented in Placco et al. (2014c). Typical uncertainties for the atmospheric parameters are 125 K for T_{eff} , 0.35 dex for $\log g$, and 0.15–0.20 dex for $[\text{Fe}/\text{H}]$, $[\text{C}/\text{Fe}]$, and $[\alpha/\text{Fe}]$.

4. Comparison with RAVE Parameters

In this section, we present a comparison between the atmospheric parameters determined by the n-SSPP and the ones from the RAVE DR5 (Kunder et al. 2017) and the RAVE-on-pipelines (Casey et al. 2017). The values used for these comparisons (Figures 5 and 6) are listed in Table 3. Also shown in the table are the parameters from RAVE DR4 (Kordopatis et al. 2013), from which the bulk of our target selection was made. The RAVE pipeline derives parameters by a χ^2 method using an extensive grid of synthetic spectra (see Zwitter et al. 2008, for further details).

4.1. RAVE DR5

The atmospheric parameters for RAVE DR5 were calculated with the DR4 stellar pipeline and calibrated using *Kepler* K2 seismic gravities, *Gaia* benchmark stars, and results obtained from high-resolution studies (see Kunder et al. 2017, for further details). Thus, we refrain from using DR4 parameters for the following analysis but list them in Table 3 nonetheless.

Figure 5 presents the results of this comparison for two different cases: (i) the full data set, regardless of RAVE quality flag values (light-gray filled squares), and (ii) the subsample of stars where the RAVE pipeline converged and the first three morphological flags indicate that the spectrum is of a normal star ($\text{QK}=0$ and $\text{c1}/\text{c2}/\text{c3}=\text{n}/\text{n}/\text{n}$ —red filled squares). The following discussion refers to the comparison between the n-SSPP values and the subsample of RAVE stars with parameters satisfying these criteria.

The left panels of Figure 5 show the differences between parameters determined by the n-SSPP ($T_{\text{eff n-SSPP}}$, $\log g_{\text{n-SSPP}}$, and $[\text{Fe}/\text{H}]_{\text{n-SSPP}}$) and from RAVE ($T_{\text{eff DR5}} - T_{\text{eff N_K}}$, $T_{\text{eff DR5 IR}} - T_{\text{eff N_K}}$, $\log g_{\text{DR5}} - \log g_{\text{N_K}}$, and $[\text{Fe}/\text{H}]_{\text{DR5-Met_N_K}}$), as a function of the RAVE DR5 spectroscopic values. Filled symbols refer to the stars observed as part of this work. The horizontal solid line in each panel is the average of the residuals, while the darker and lighter shaded areas represent the 1σ and 2σ regions, respectively. The right panels show histograms of the residuals between the n-SSPP and RAVE parameters. Each panel also lists the number of stars, the average offset, and the scatter determined from a Gaussian fit to the residual distribution.

There are large deviations when comparing T_{eff} values from RAVE and the n-SSPP. Our determinations are consistently higher, in particular for $T_{\text{eff}} < 4750$ K. The zero-point offset on the residuals is 127 K and the scatter is 251 K. There is a somewhat good agreement between these estimates in the $[4500:5200]$ K range, and it is also possible to notice an upward trend on the residuals for decreasing $T_{\text{eff DR5}}$ values. The RAVE DR5 catalog also provides temperature estimates based on the infrared flux method of Casagrande et al. (2010) ($T_{\text{eff DR5 IR}}$). These are in better agreement with the n-SSPP values, showing a zero-point offset on the residuals of just 62 K, and a scatter of 111 K.

The $\log g$ comparison presents a more significant trend, with a zero-point offset on the residuals of 0.5 dex and a scatter of 1.1 dex.

The behavior of the metallicity residuals follows similar trends as the T_{eff} and $\log g$. This is expected, since the spectral features used for $[\text{Fe}/\text{H}]$ estimates also change with temperature. The zero-point offset on the residual distribution is -0.1 dex and the scatter is 0.6 dex.

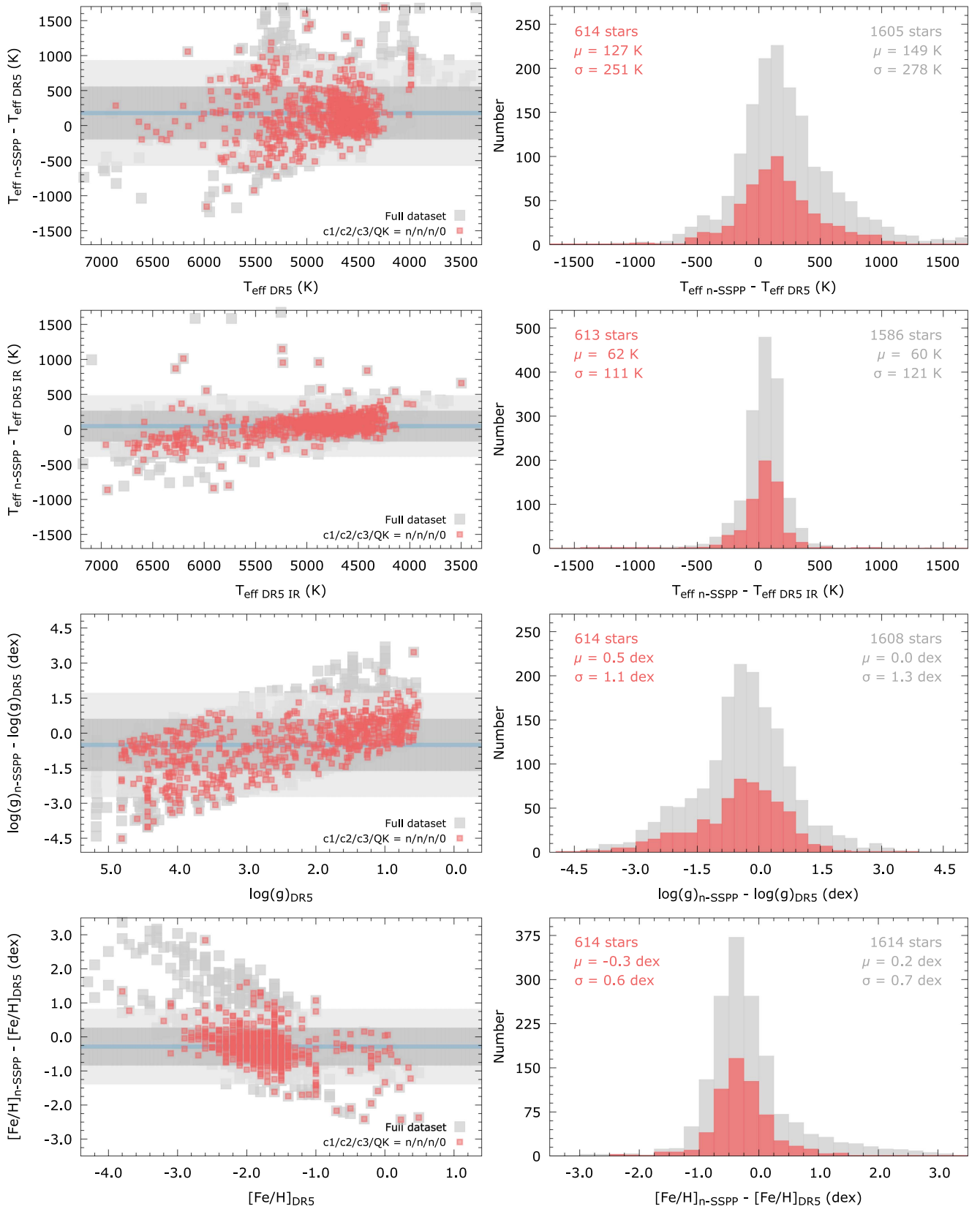


Figure 5. Left panels: differences between the atmospheric parameters determined by the n-SSPP, $T_{\text{eff n-SSPP}}$, $\log g_{\text{n-SSPP}}$, and $[\text{Fe}/\text{H}]_{\text{n-SSPP}}$, and the values from RAVE, $T_{\text{eff DR5}}$, $T_{\text{eff DR5IR}}$, $\log g_{\text{DR5}}$, and $[\text{Fe}/\text{H}]_{\text{DR5}}$, reported by Kunder et al. (2017), as a function of the RAVE spectroscopic values. Filled symbols refer to the full sample of observed stars with determined parameters (light-gray) and a subsample with constraints on quality flags (red—see the text for details). The horizontal solid line is the average of the residuals, while the darker and lighter shaded areas represent the 1 σ and 2 σ regions, respectively. Right panels: histograms of the residuals between the n-SSPP and RAVE parameters shown in the left panels. Each panel also lists the average offset and scatter determined from a Gaussian fit.

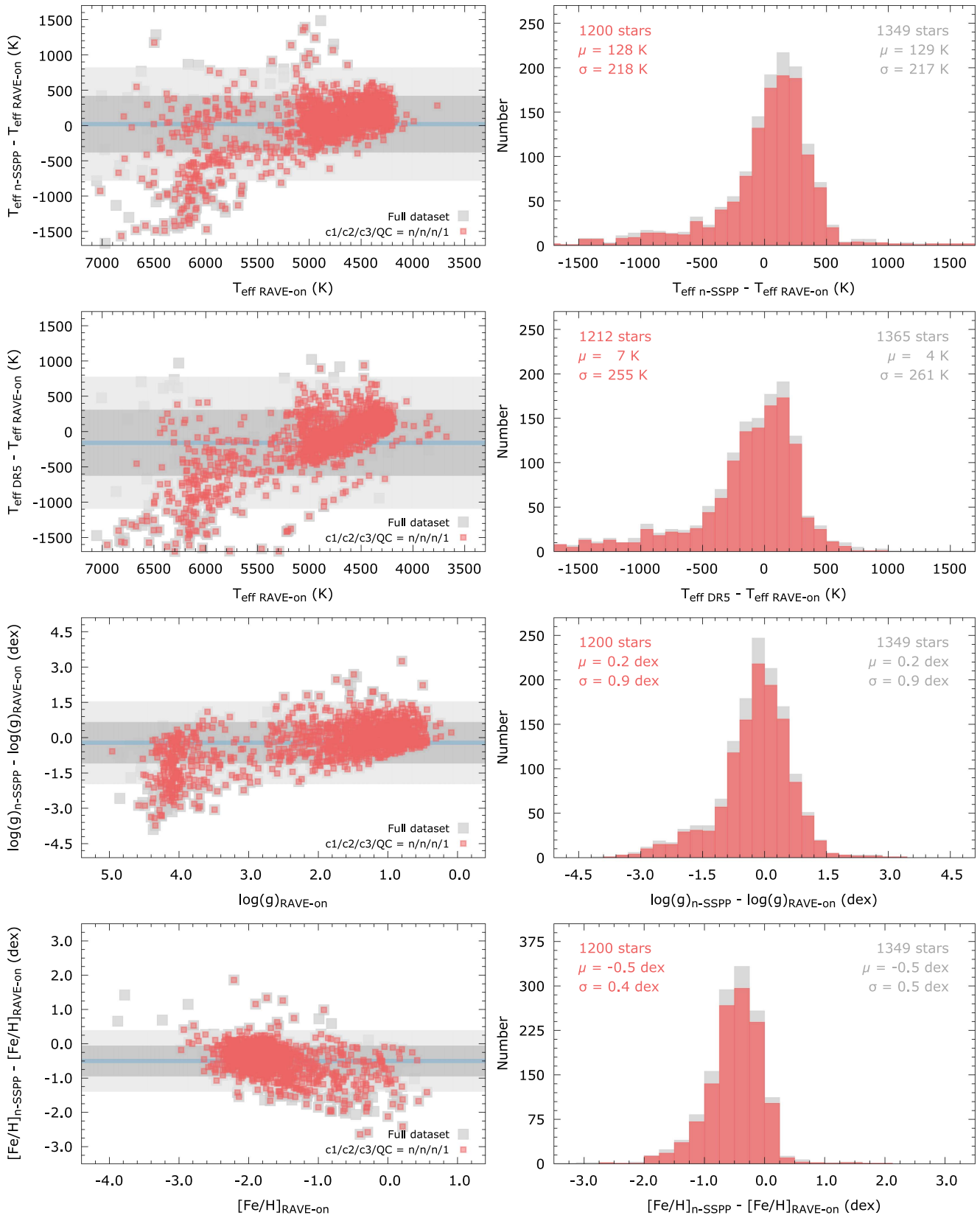


Figure 6. Left panels: differences between the atmospheric parameters determined by the n-SSPP, $T_{\text{eff n-SSPP}}$, $\log g_{\text{n-SSPP}}$, and $[\text{Fe}/\text{H}]_{\text{n-SSPP}}$, and the values from RAVE-on, $T_{\text{eff RAVE-on}}$, $\log g_{\text{RAVE-on}}$, and $[\text{Fe}/\text{H}]_{\text{RAVE-on}}$, reported by Casey et al. (2017), as a function of the RAVE-on spectroscopic values. Filled symbols refer to the full sample of observed stars with determined parameters (light-gray) and a subsample with constraints on quality flags (red—see the text for details). The horizontal solid line is the average of the residuals, while the darker and lighter shaded areas represent the 1σ and 2σ regions, respectively. Right panels: histograms of the residuals between the n-SSPP and RAVE parameters shown in the left panels. Each panel also lists the average offset and scatter determined from a Gaussian fit.

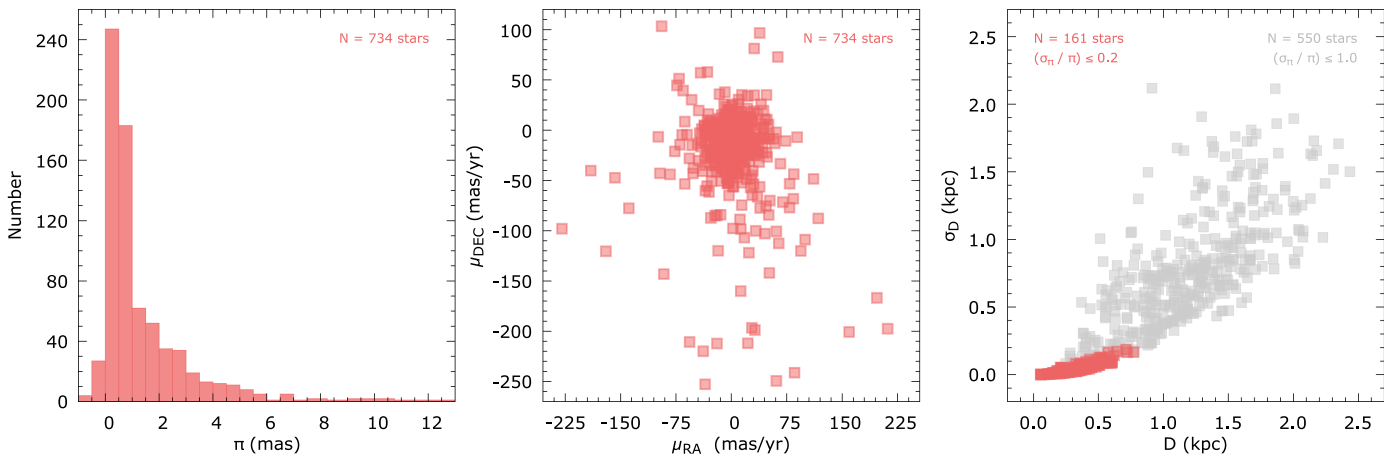


Figure 7. Left panel: parallax distribution for the observed RAVE stars found in the *Gaia* TGAS catalog. Middle panel: Proper motions for these stars. Right panel: derived distances (with associated errors) from Astraatmadja & Bailer-Jones (2016), for stars with $\sigma_\pi/\pi \leq 1.0$ (gray symbols) and $\sigma_\pi/\pi \leq 0.2$ (red symbols).

4.2. RAVE-on

The RAVE-on catalog of stellar atmospheric parameters presents a re-analysis of RAVE spectra using the data-driven code *The Cannon* (Ness et al. 2015), using data models from APOGEE and *Kepler* K2 (see Casey et al. 2017, for further details). A comparison between the RAVE-on parameters and the n-SSPP parameters is presented in Figure 6, for the same cases shown above: (i) The full data set, regardless of RAVE-on quality flag values (light-gray filled squares), and (ii) The subsample of stars where the RAVE-on pipeline converged and the first three morphological flags indicate that the spectrum is of a normal star ($QC=1$ and $c1/c2/c3=n/n/n$ —red filled squares).

The left panels of Figure 6 show the differences between parameters determined by the n-SSPP ($T_{\text{eff n-SSPP}}$, $\log g_{\text{n-SSPP}}$, and $[\text{Fe}/\text{H}]_{\text{n-SSPP}}$) and from RAVE-on ($T_{\text{eff RAVE-on}}$, $\log g_{\text{RAVE-on}}$, and $[\text{Fe}/\text{H}]_{\text{RAVE-on}}$), as a function of the RAVE-on values. Also shown is the comparison between the effective temperatures in RAVE DR5 and RAVE-on. Filled symbols refer to the stars observed as part of this work. The horizontal solid line in each panel is the average of the residuals, while the darker and lighter shaded areas represent the 1σ and 2σ regions, respectively. The right panels show histograms of the residuals between the n-SSPP and RAVE parameters. Each panel also lists the average offset and scatter determined from a Gaussian fit to the residual distribution.

The deviations, when comparing T_{eff} values from RAVE-on and the n-SSPP are large, in particular for $T_{\text{eff}} > 5000$ K. The zero-point offset in the residuals and the scatter (128 K and 218 K, respectively) are slightly smaller than RAVE DR5 versus n-SSPP, as seen in Figure 5. For $T_{\text{eff}} < 5000$ K, the spread between the determinations is smaller, but there is a noticeable offset, with the n-SSPP temperatures being higher when compared to RAVE-on. We also compared the RAVE-on temperatures with the values from RAVE DR5. The correlation is worse, even though the zero-point offset in the residuals is just 7 K, and the scatter is 255 K. Still, similar to the other temperature comparisons, the agreement is somewhat better in the [4500:5200] K range.

The $\log g$ comparison exhibits better agreement than the one between the n-SSPP and RAVE DR5, with a zero-point offset of 0.2 dex and a scatter of 0.9 dex. The scatter is mostly driven by values with $\log g_{\text{RAVE-on}} \gtrsim 3.0$.

The behavior of the metallicity residuals follows the same trends as the T_{eff} and $\log g$. The agreement is similar to the comparison between the n-SSPP and the RAVE DR5 values shown in Figure 5. The zero-point offset in the residual distribution is -0.5 dex and the scatter is 0.4 dex. The n-SSPP values are consistently smaller than the RAVE-on determinations, with a larger scatter for $[\text{Fe}/\text{H}]_{\text{RAVE-on}} \gtrsim -1.0$.

5. Sample Stars Observed with *Gaia*

We searched the Tycho-*Gaia* Astrometric Solution database (TGAS; *Gaia* Collaboration et al. 2016; Lindegren et al. 2016), and found 734 matches with stars in our sample. Figure 7 (left and middle panels) shows the distribution of the parallaxes and proper motions for these stars. Distances (and associated errors) were taken from the catalog of Astraatmadja & Bailer-Jones (2016), who inferred distances for the TGAS objects using not only observed parallaxes and their uncertainties, but also an anisotropic prior derived from the observability of stars in a Milky Way model (see Bailer-Jones 2015, for further details). The right panel of Figure 7 shows distances (and associated errors) for stars with $\sigma_\pi/\pi \leq 0.2$ and $\sigma_\pi/\pi \leq 1.0$. Although the latter is a fairly relaxed constraint, we chose it in order to have a larger sample of stars to exemplify our improved selection criteria (see below). Because of that, distances are limited to $D \leq 2.5$ kpc. Table 4 lists, for the 734 stars in common with TGAS, the *Gaia* ID, G magnitude, proper motions ($\mu_{\text{R.A.}}$ and $\mu_{\text{dec.}}$), and parallaxes (π). Distances and errors inferred from the Milky Way prior were taken from the Astraatmadja & Bailer-Jones (2016) catalog.

Having kinematic information for these stars in addition to atmospheric parameters is a valuable tool for better pre-selecting low-metallicity stars for spectroscopic follow up. Using the information provided by TGAS, we were able to calculate the Cartesian coordinates and transverse velocities for the sample with $\sigma_\pi/\pi \leq 1.0$. The upper panels of Figure 8 show the behavior of the height above the Galactic plane (Z , in kpc) as a function of the transverse velocity (V_T , in km s^{-1}), for three metallicity regimes. The shaded areas roughly mark the region occupied by thin-disk stars (± 500 pc; Recio-Blanco et al. 2014) and typical transverse velocities for thin-disk stars. Also shown are the V_T cumulative distribution functions (CDFs). Values on each panel represent the fraction of stars in each $[\text{Fe}/\text{H}]$ regime with $V_T \geq 75 \text{ km s}^{-1}$ and

Table 4
Gaia/TGAS Parameters

Star Name (RAVE)	ID (<i>GAIA</i>)	G (mag)	$\mu_{\text{R.A.}}$ (mas yr $^{-1}$)	$\sigma_{\mu_{\text{R.A.}}}$ (mas yr $^{-1}$)	$\mu_{\text{decl.}}$ (mas yr $^{-1}$)	$\sigma_{\mu_{\text{decl.}}}$ (mas yr $^{-1}$)	π (mas)	σ_{π} (mas)	D (kpc)	σ_D (kpc)	V_T (km s $^{-1}$)	Z (kpc)
J000245.9–325734	2313475887653200384	11.75	78.862	0.804	–53.267	0.857	0.600	0.340	1.108	0.811	279	–0.595
J000414.3–265709	2333779366292490240	10.39	8.502	0.152	–14.463	0.082	0.380	0.280	1.454	1.281	100	1.185
J000415.8–581553	4919110843943100416	10.22	11.667	0.524	–7.546	0.535	0.170	0.250	2.133	2.027	78	–2.015
J000417.4–124503	2421324921637437952	12.08	20.737	1.761	–48.790	1.004	0.740	0.540	0.842	0.715	210	–0.314
J000438.4–540134	4923965909334259712	12.01	22.633	0.381	–13.198	0.397	0.170	0.220	2.379	2.264	255	2.092

(This table is available in its entirety in machine-readable form.)

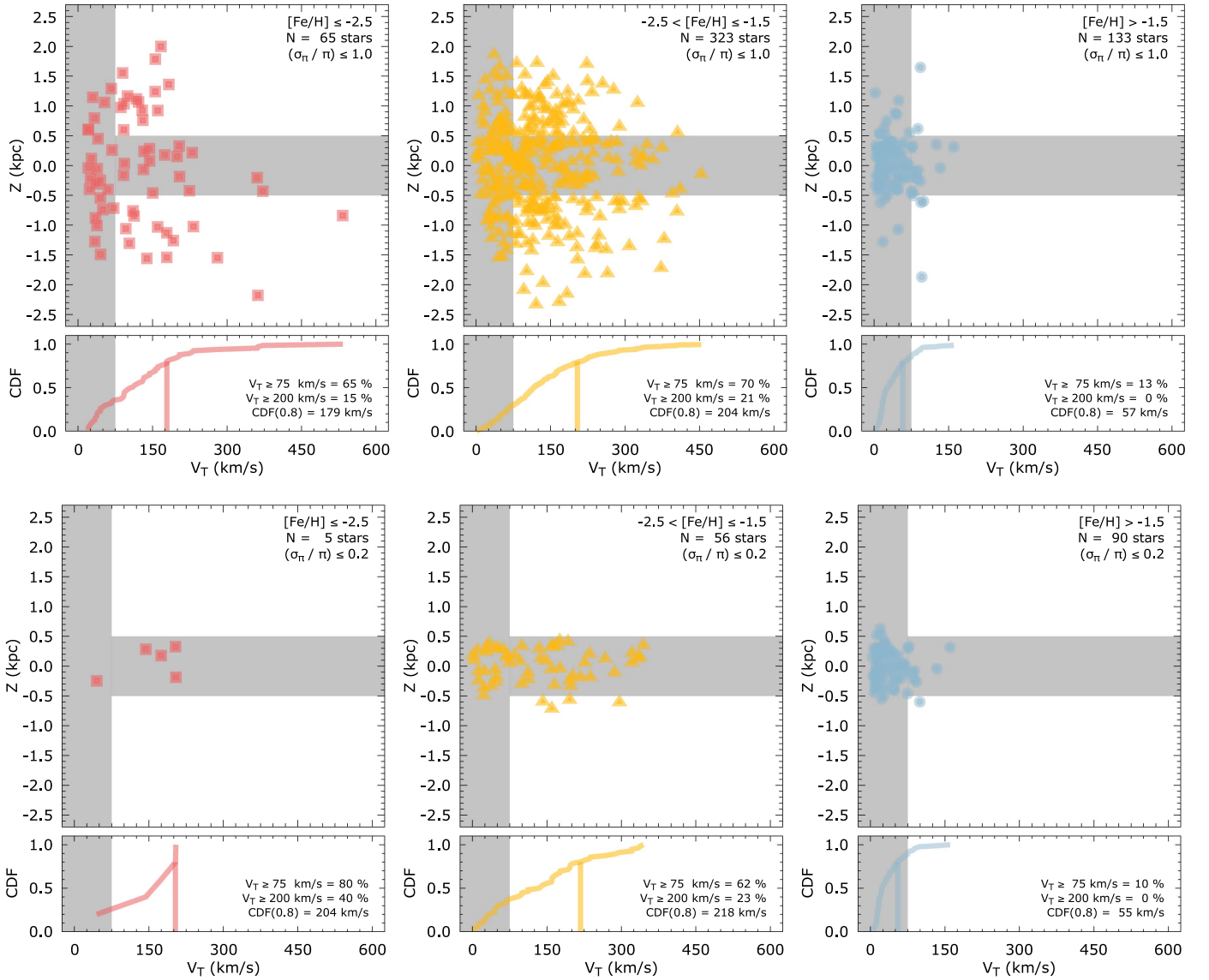


Figure 8. Distance from the Galactic plane (Z , in kpc), as a function of the transverse velocity (V_T , in km s^{-1}), for three metallicity regimes. The horizontal shaded area roughly marks the region potentially occupied by thin-disk stars in the Galaxy (± 500 pc), and the vertical shaded area represents typical transverse velocities occupied by thin-disk stars (see the text for details). Also shown are the V_T cumulative distribution functions for the $[\text{Fe}/\text{H}]$ intervals. The values shown in each panel represent the fraction of stars for $V_T \geq 75 \text{ km s}^{-1}$, and $V_T \geq 200 \text{ km s}^{-1}$, and the V_T value where the CDF reaches a fraction of 80%. The upper panels show the stars with accepted distances from TGAS ($\sigma_\pi/\pi \leq 1.0$), and the lower panel shows a more restricted error cut on parallaxes ($\sigma_\pi/\pi \leq 0.2$).

$V_T \geq 200 \text{ km s}^{-1}$, and also the V_T value where the CDF reaches a fraction of 80%. The bottom panels of Figure 8 show the same quantities, using a more restrictive error cut on parallaxes ($\sigma_\pi/\pi \leq 0.2$; 151 stars).

From inspection of Figure 8, it can be seen that the transverse velocity is an effective additional constraint to select low-metallicity stars. The CDF for the high-metallicity regime reaches 80% at $V_T = 57 \text{ km s}^{-1}$, while the more metal-poor regimes only reach 80% at $V_T \geq 180 \text{ km s}^{-1}$. In fact, at $V_T \geq 200 \text{ km s}^{-1}$, there are no stars in our sample with $[\text{Fe}/\text{H}] > -1.5$. The same applies to the distance-limited sample shown on the lower panels of Figure 8. By application of a search criteria in V_T (but not in Z), one can successfully search for stars belonging to the halo population, but currently located close to the Galactic plane.

To roughly quantify the improvement in the search for low-metallicity stars using the transverse velocity, we use the V_T and $[\text{Fe}/\text{H}]$ for the 550 stars shown in the right panel of

Figure 7. Within those, 82% have $[\text{Fe}/\text{H}] \leq -1.0$ and 50% have $[\text{Fe}/\text{H}] \leq -2.0$. By selecting stars with $V_T \geq 75 \text{ km/s}$ and $V_T \geq 200 \text{ km/s}$, these fractions would increase to 97%/58% and 100%/60%, respectively, albeit with the disadvantage that a kinematic bias is injected into the resulting sample. We caution the reader that the present sample *was chosen* to include only low-metallicity stars based on RAVE parameters. Nonetheless, the quantifiable improvements in the fractions suggest that these constraints should also be robust in non- $[\text{Fe}/\text{H}]$ -biased samples, and can be used to tailor future searches for metal-poor stars.

6. Carbon and α -element Abundances

In a sample of low-metallicity stars, one should expect an increasing fraction of CEMP ($[\text{Fe}/\text{H}] \leq -1.0$ and $[\text{C}/\text{Fe}] \geq +0.7$) stars for decreasing metallicities (Rossi et al. 1999, 2005; Beers & Christlieb 2005; Placco

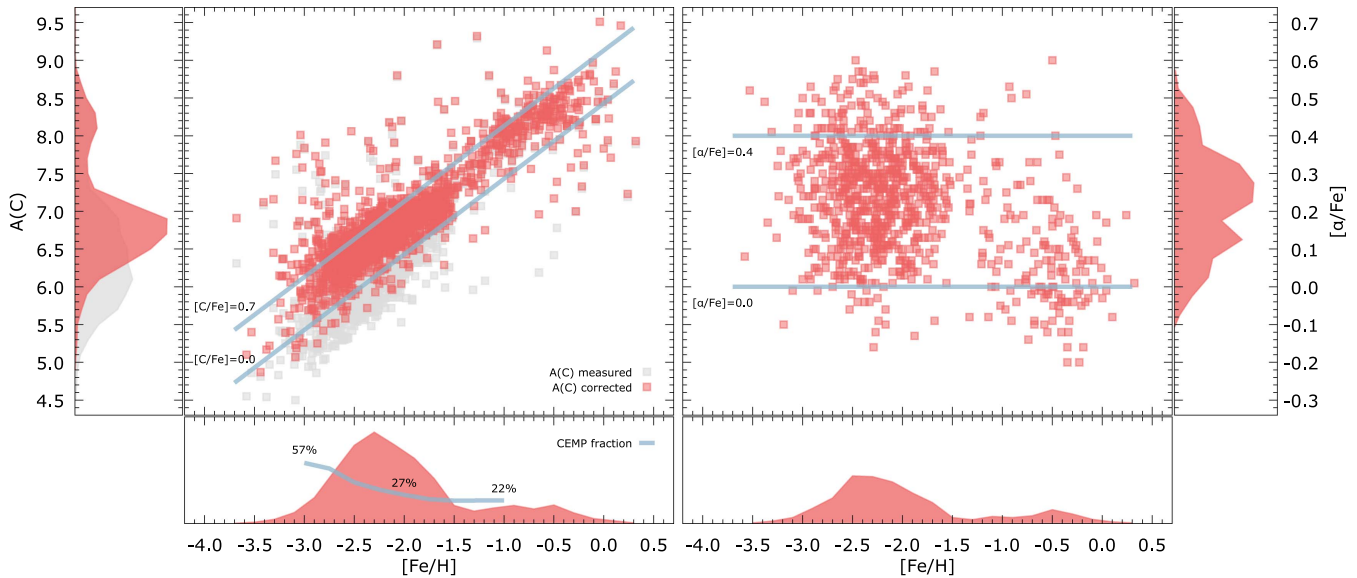


Figure 9. Absolute carbon ($A(C)$), measured and corrected—left panel), and relative α -element abundances (right panel), as a function of the metallicity calculated by the n-SSPP. The side and lower panels show the marginalized distributions for each quantity. The solid line in the lower panel shows the cumulative CEMP fractions for the stars with $-3.0 \leq [Fe/H] \leq -1.0$.

Table 5
Group Assignments for CEMP Stars

Star Name (RAVE)	V (mag)	T_{eff} (K)	[Fe/H]	[C/Fe]	[C/Fe] _c	$A(C)_c$	Group
J001548.1–625321	11.04	4711	-2.63	-0.01	+0.70	6.50	II
J002330.7–163143	12.28	5542	-2.40	+0.76	+0.77	6.80	I
J004539.3–745729	11.67	5049	-2.24	+1.24	+1.37	7.56	I
J005419.7–061155	13.07	4897	-2.59	+0.30	+0.72	6.56	II
J011553.2–733050	10.81	6422	-1.56	+0.83	+0.83	7.70	I

(This table is available in its entirety in machine-readable form.)

et al. 2010, 2011). Among the 1606 stars observed in this work for which carbon abundances could be determined, we identified 106 CEMP stars, before applying the carbon corrections of Placco et al. (2014c), and 306 CEMP stars, after corrections were applied. Because RAVE does not provide carbon abundances, we have the opportunity to add yet another selection criteria when assembling target lists for high-resolution spectroscopic follow up.

Figure 9 shows, on the left side, the absolute carbon abundances ($A(C)$),²⁵ measured and corrected), as a function of the metallicity calculated by the n-SSPP. The side and lower panels show the marginalized distributions for each quantity. The right side of Figure 9 shows the α -element abundance ratios as a function of the metallicity. The $[\alpha/Fe]$ ratio behaves similarly to the sample of Cayrel et al. (2004), with values typically ranging from 0.0 to +0.4.

The sample observed in this work also provides for an independent (and unbiased) calculation of the fractions of carbon-enhanced stars as a function of metallicity. Results are shown in the bottom-left panel of Figure 9, where the solid line represents the cumulative CEMP fractions for stars with $-3.0 \leq [Fe/H] \leq -1.0$. The fraction for $[Fe/H] \leq -2.0$ ($27 \pm 3\%$)²⁶ agrees within uncertainties with the $20 \pm 13\%$

fraction reported by Placco et al. (2014c) but is somewhat higher than the $13 \pm 1\%$ fraction reported by Lee et al. (2013). For $[Fe/H] \leq -3.0$, the fraction found in this work ($57^{+13}_{-14}\%$) is higher than both Placco et al. ($43 \pm 5\%$) and Lee et al. ($23 \pm 3\%$).

The CEMP stars identified in this work can be further subclassified, based on their position in the Yoon–Beers $A(C)$ versus $[Fe/H]$ diagram, following Yoon et al. (2016). Roughly, one would expect to find (assuming $[Fe/H] \leq -1.0$ and $[C/Fe] \geq +0.7$) CEMP-*s* (or CEMP-*i*) stars for $-3.5 \lesssim [Fe/H] \lesssim -2.5$ and $A(C) \gtrsim 7.25$ or $[Fe/H] \gtrsim -2.5$, $A(C) \lesssim 7.25$, and $[C/Fe] \leq +1.5$ (Group II) or $[C/Fe] > +1.5$ (Group III). Based on these, there are 169 CEMP Group I, 131 CEMP Group II, and 6 CEMP Group III stars. Table 5 lists the main parameters for all 306 CEMP stars, including the assignment between Groups I/II/III.

The upper panel of Figure 10 shows the distribution of CEMP stars among these groups. We note that these limits and classifications aim to provide a first-step criteria for selection, and the region at $[Fe/H] \sim -2.5$ is where the groups in Yoon et al. (2016) overlap. The enhancement in carbon in Group I stars is the result of external pollution from an AGB companion in a binary system. Because of that, these objects are not suitable to probe the chemical evolution of the Galaxy. Groups II and III, in contrast, are believed to describe stars

²⁵ $A(C) = \log(N_C/N_{\text{H}}) + 12$.

²⁶ Uncertainties in the fractions represent the Wilson score confidence intervals (Wilson 1927). See Yoon et al. (2018) for further details.

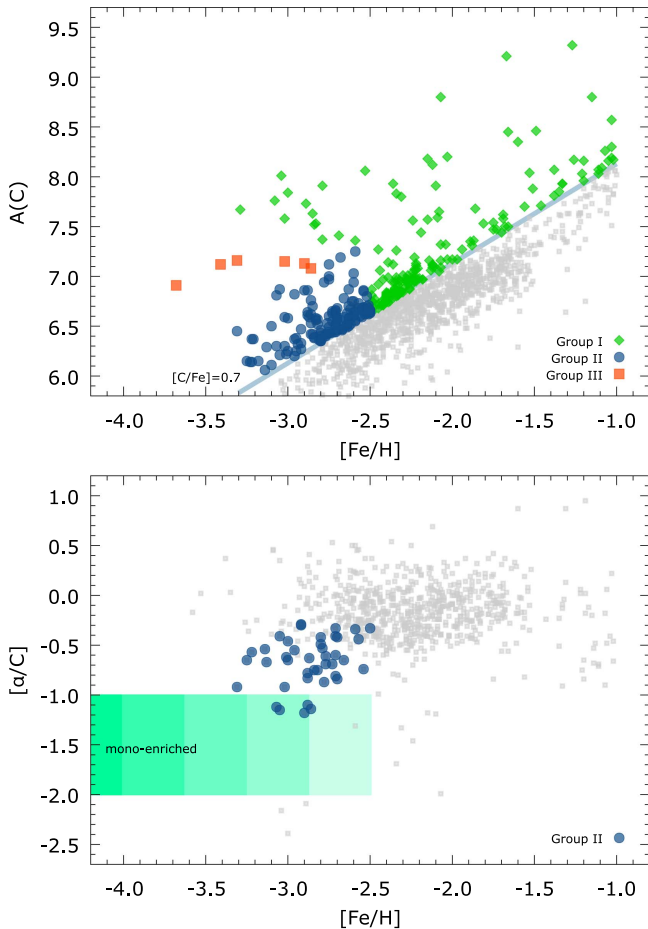


Figure 10. Upper panel: $A(C)$, as a function of the n-SSPP metallicity, for stars with $[Fe/H] \leq -1.0$. CEMP stars belonging to Groups I, II, and III are identified, following the criteria described in the text. Lower panel: $[\alpha/C]$ abundance ratio. The shaded area outlines the region where mono-enriched second-generation stars would preferably be found.

formed from gas clouds that were enriched by early SNe events from massive stars.

Hartwig et al. (2018) argue that that the so-called *mono-enriched* stars (indicating a single first-star progenitor) can be found at metallicities as high as $[Fe/H] \sim -2.0$ and can be separated from other *multiple-enriched* stars, based on the $[Mg/C]$ ratio. Because the n-SSPP calculates $[\alpha/Fe]$, in principle, the $[\alpha/C]$ ratio can be used to identify true mono-enriched stars. The lower panel of Figure 10 shows the distribution of this quantity for the stars in the sample, highlighting the CEMP Group II stars. Note that all six CEMP Group III were observed with ESO/NTT; hence, there are no $[\alpha/Fe]$ determinations available for these stars. The shaded area outlines the region where mono-enriched second-generation stars would preferably be found (Hartwig et al. 2018).

7. Conclusions

We have presented results from a medium-resolution ($R \sim 1200\text{--}2000$) spectroscopic follow up of low-metallicity stars selected from the RAVE database. Our observing campaign ran from semester 2014A to 2017A and used six different telescope/instrument configurations, in both the southern and northern hemispheres. Atmospheric parameters and abundances for carbon and the α -elements were calculated using our well-tested n-SSPP pipeline. From the 1694 unique

stars observed, 1413 were confirmed to be metal-poor ($[Fe/H] \leq -1.0$), and 306 were carbon-enhanced ($[C/Fe] \geq +0.7$), after evolutionary corrections have been applied.

Comparison with atmospheric-parameter estimates from RAVE DR5 and RAVE-on revealed discrepancies, in particular for temperatures, with a 127 K zero-point offset in the residual distribution, and a 251 K scatter (n-SSPP versus RAVE DR5). These differences led to similar inconsistencies in $\log g$ and $[Fe/H]$, resulting in 202 stars with $[Fe/H]_{n\text{-SSPP}} \geq -1.0$ being included in our sample. The agreement is somewhat better between the RAVE-on values and the n-SSPP, however, with large scatter for $T_{\text{effRAVE-on}} \gtrsim 5000$ K and $\log g_{\text{RAVE-on}} \gtrsim 3.0$. A forthcoming paper will compare the n-SSPP determinations with values from ongoing high-resolution spectroscopic follow up by the R-Process Alliance; then, we will be able to better assess the nature of the differences presented in this work.

A search in the *Gaia*/TGAS database revealed matches for 734 stars observed in this work. Based on a height above the Galactic plane versus transverse velocity diagram, we show that these kinematical properties can be further used to pre-select low-metallicity stars as well, increasing the success rate of similar spectroscopic follow-ups in the future.

The atmospheric parameters and carbon abundances determined by this work not only characterize the sample of halo stars but also serve as a stepping stone for constructing target lists for a variety of follow-up studies (e.g., Hansen et al. 2018). In this regard, the most metal-poor stars identified (including the CEMP Group III and the *mono-enriched stars*) have already been followed-up with high-resolution spectroscopy for detailed abundance studies. One *r-II* star with detected uranium (Placco et al. 2017), a bright *r-II* star at $[Fe/H] \sim -2$ (Sakari et al. 2018), and the first *r + s* star (showing the *combined* signature of the *r*-process and *s*-process; M. Gull et al. 2018, in preparation) have also been found. Furthermore, Placco et al. (2016b) used a UMP star from RAVE to help constrain the mass distribution of the first stars in the universe. This work is ongoing, with more publications to follow in due course. Overall, these efforts will continue to expand our understanding of the nucleosynthesis of the elements and early chemical evolution, which forms the basis for understanding star- and galaxy-formation in the early universe.

The authors acknowledge partial support for this work from grant PHY 14-30152; Physics Frontier Center/JINA Center for the Evolution of the Elements (JINA-CEE), awarded by the US National Science Foundation. S.R. acknowledges partial support from FAPESP, CAPES/PROEX, and CNPq. Y.S.L. acknowledges support from the National Research Foundation (NFR) of Korea grant funded by the Ministry of Science and ICT (No.2017R1A5A1070354, NRF-2015R1C1A1A02036658, and NRF-2018R1A2B6003961). Based on observations at Kitt Peak National Observatory, National Optical Astronomy Observatory (NOAO Prop. IDs: 14A-0323, 14B-0231, 15A-0071, 15B-0071, 17A-0295), which is operated by the Association of Universities for Research in Astronomy (AURA) under cooperative agreement with the National Science Foundation. The authors are honored to be permitted to conduct astronomical research on Iolkam Du'ag (Kitt Peak), a mountain with particular significance to the Tohono O'odham. Based on observations obtained at the

Gemini Observatory (Prop. IDs: GN-2015A-Q-401, GS-2015A-Q-205), which is operated by the Association of Universities for Research in Astronomy, Inc., under a cooperative agreement with the NSF on behalf of the Gemini partnership: the National Science Foundation (United States), the National Research Council (Canada), CONICYT (Chile), Ministerio de Ciencia, Tecnología e Innovación Productiva (Argentina), and Ministério da Ciência, Tecnologia e Inovação (Brazil). Based on observations obtained at the Southern Astrophysical Research (SOAR) telescope (Prop. IDs: 2014B-0231, 2015A-0071, 2015B-0020, 2016A-0019, 2017A-0016), which is a joint project of the Ministério da Ciência, Tecnologia, e Inovação (MCTI) da República Federativa do Brasil, the U.S. National Optical Astronomy Observatory (NOAO), the University of North Carolina at Chapel Hill (UNC), and Michigan State University (MSU). Based on observations collected at the European Organisation for Astronomical Research in the southern hemisphere under ESO programme(s) 095.D-0202(A), 096.D-0018(A), 097.D-0196(A), 098.D-0434(A), and 099.D-0428(A). This work has made use of data from the European Space Agency (ESA) mission *Gaia* (<http://www.cosmos.esa.int/gaia>), processed by the *Gaia* Data Processing and Analysis Consortium (DPAC), <http://www.cosmos.esa.int/web/gaia/dpac/consortium>).

Funding for the DPAC has been provided by national institutions, in particular the institutions participating in the *Gaia* Multilateral Agreement. This research has made use of NASA's Astrophysics Data System Bibliographic Services; the arXiv pre-print server operated by Cornell University; the SIMBAD database hosted by the Strasbourg Astronomical Data Center; and the online Q&A platform [stackoverflow](http://stackoverflow.com/) (<http://stackoverflow.com/>).

Software: awk (Aho et al. 1987), gnuplot (Williams & Kelley 2015), IRAF (Tody 1986, 1993), n-SSPP (Beers et al. 2014), R-project (R Core Team 2015), sed (McMahon 1979).

ORCID iDs

Vinicius M. Placco  <https://orcid.org/0000-0003-4479-1265>
 Timothy C. Beers  <https://orcid.org/0000-0003-4573-6233>
 Rafael M. Santucci  <https://orcid.org/0000-0002-7529-1442>
 Georges Kordopatis  <https://orcid.org/0000-0002-9035-3920>
 Young Sun Lee  <https://orcid.org/0000-0001-5297-4518>
 Anna Frebel  <https://orcid.org/0000-0002-2139-7145>
 Terese T. Hansen  <https://orcid.org/0000-0001-6154-8983>
 Erika M. Holmbeck  <https://orcid.org/0000-0002-5463-6800>
 Ian U. Roederer  <https://orcid.org/0000-0001-5107-8930>
 Charli M. Sakari  <https://orcid.org/0000-0002-5095-4000>

References

Abbott, B. P., Abbott, R., Abbott, T. D., et al. 2017, *ApJL*, **848**, L12
 Aho, A. V., Kernighan, B. W., & Weinberger, P. J. 1987, *The AWK Programming Language* (Boston, MA: Addison-Wesley)
 Aoki, W., Beers, T. C., Christlieb, N., et al. 2007, *ApJ*, **655**, 492
 Astraatmadja, T. L., & Bailer-Jones, C. A. L. 2016, *ApJ*, **833**, 119
 Bailer-Jones, C. A. L. 2015, *PASP*, **127**, 994
 Barklem, P. S., Christlieb, N., Beers, T. C., et al. 2005, *A&A*, **439**, 129
 Beers, T. C., & Christlieb, N. 2005, *ARA&A*, **43**, 531
 Beers, T. C., Norris, J. E., Placco, V. M., et al. 2014, *ApJ*, **794**, 58
 Beers, T. C., Placco, V. M., Carollo, D., et al. 2017, *ApJ*, **835**, 81
 Beers, T. C., Preston, G. W., & Shectman, S. A. 1985, *AJ*, **90**, 2089
 Beers, T. C., Preston, G. W., & Shectman, S. A. 1992, *AJ*, **103**, 1987
 Bessell, M., Collett, R., Keller, S., et al. 2015, *ApJL*, **806**, L16

Burbidge, E. M., Burbidge, G. R., Fowler, W. A., & Hoyle, F. 1957, *RvMP*, **29**, 547
 Cameron, A. G. W. 1957, *PASP*, **69**, 201
 Casagrande, L., Ramírez, I., Meléndez, J., Bessell, M., & Asplund, M. 2010, *A&A*, **512**, A54
 Casey, A. R., Hawkins, K., Hogg, D. W., et al. 2017, *ApJ*, **840**, 59
 Cayrel, R., Depagne, E., Spite, M., et al. 2004, *A&A*, **416**, 1117
 Chiaki, G., Tominaga, N., & Nozawa, T. 2017, *MNRAS*, **472**, L115
 Christlieb, N., Beers, T. C., Barklem, P. S., et al. 2004, *A&A*, **428**, 1027
 Christlieb, N., Bessell, M. S., Beers, T. C., et al. 2002, *Natur*, **419**, 904
 Christlieb, N., Schörck, T., Frebel, A., et al. 2008, *A&A*, **484**, 721
 Cooke, R., & Madau, P. 2014, *ApJ*, **791**, 116
 Cooke, R., Pettini, M., & Murphy, M. T. 2012, *MNRAS*, **425**, 347
 Demarque, P., Woo, J.-H., Kim, Y.-C., & Yi, S. K. 2004, *ApJS*, **155**, 667
 Dotter, A., Chaboyer, B., Jevremović, D., et al. 2008, *ApJS*, **178**, 89
 Drout, M. R., Piro, A. L., Shappee, B. J., et al. 2017, *Sci*, **358**, 1570
 Frebel, A., Aoki, W., Christlieb, N., et al. 2005, *Natur*, **434**, 871
 Frebel, A., Chiti, A., Ji, A. P., Jacobson, H. R., & Placco, V. M. 2015, *ApJL*, **810**, L27
 Frebel, A., Christlieb, N., Norris, J. E., et al. 2006, *ApJ*, **652**, 1585
 Frebel, A., & Norris, J. E. 2015, *ARA&A*, **53**, 631
 Frebel, A., Simon, J. D., & Kirby, E. N. 2014, *ApJ*, **786**, 74
 Gaia Collaboration, Prusti, T., de Bruijne, J. H. J., et al. 2016, *A&A*, **595**, A1
 Hansen, T., Hansen, C. J., Christlieb, N., et al. 2014, *ApJ*, **787**, 162
 Hansen, T., Hansen, C. J., Christlieb, N., et al. 2015, *ApJ*, **807**, 173
 Hansen, T. T., Holmbeck, E. M., Beers, T. C., et al. 2018, *ApJ*, **858**, 92
 Hartwig, T., Yoshida, N., Magg, M., et al. 2018, *MNRAS*, Advanced Access
 Ito, H., Aoki, W., Beers, T. C., et al. 2013, *ApJ*, **773**, 33
 Jeon, M., Besla, G., & Bromm, V. 2017, *ApJ*, **848**, 85
 Ji, A. P., Frebel, A., Chiti, A., & Simon, J. D. 2016, *Natur*, **531**, 610
 Keller, S. C., Bessell, M. S., Frebel, A., et al. 2014, *Natur*, **506**, 463
 Keller, S. C., Schmidt, B. P., Bessell, M. S., et al. 2007, *PASA*, **24**, 1
 Kordopatis, G., Gilmore, G., Steinmetz, M., et al. 2013, *AJ*, **146**, 134
 Kunder, A., Kordopatis, G., Steinmetz, M., et al. 2017, *AJ*, **153**, 75
 Lattimer, J. M., & Schramm, D. N. 1974, *ApJL*, **192**, L145
 Lee, Y. S., Beers, T. C., Masseron, T., et al. 2013, *AJ*, **146**, 132
 Lee, Y. S., Beers, T. C., Sivarani, T., et al. 2008a, *AJ*, **136**, 2022
 Lee, Y. S., Beers, T. C., Sivarani, T., et al. 2008b, *AJ*, **136**, 2050
 Lindgren, L., Lammers, U., Bastian, U., et al. 2016, *A&A*, **595**, A4
 Matijević, G., Zwitter, T., Bienaymé, O., et al. 2012, *ApJS*, **200**, 14
 McMahon, L. E. 1979, *UNIX Programming Manual*, Vol. 2 (7th ed.; Murray Hill: Bell Telephone Laboratories)
 Ness, M., Hogg, D. W., Rix, H.-W., Ho, A. Y. Q., & Zasowski, G. 2015, *ApJ*, **808**, 16
 Norris, J. E., Bessell, M. S., Yong, D., et al. 2013, *ApJ*, **762**, 25
 Placco, V. M., Beers, T. C., Ivans, I. I., et al. 2015a, *ApJ*, **812**, 109
 Placco, V. M., Beers, T. C., Reggiani, H., & Meléndez, J. 2016a, *ApJL*, **829**, L24
 Placco, V. M., Beers, T. C., Roederer, I. U., et al. 2014a, *ApJ*, **790**, 34
 Placco, V. M., Frebel, A., Beers, T. C., et al. 2013, *ApJ*, **770**, 104
 Placco, V. M., Frebel, A., Beers, T. C., et al. 2014b, *ApJ*, **781**, 40
 Placco, V. M., Frebel, A., Beers, T. C., et al. 2016b, *ApJ*, **833**, 21
 Placco, V. M., Frebel, A., Beers, T. C., & Stancliffe, R. J. 2014c, *ApJ*, **797**, 21
 Placco, V. M., Frebel, A., Lee, Y. S., et al. 2015b, *ApJ*, **809**, 136
 Placco, V. M., Holmbeck, E. M., Frebel, A., et al. 2017, *ApJ*, **844**, 18
 Placco, V. M., Kennedy, C. R., Beers, T. C., et al. 2011, *AJ*, **142**, 188
 Placco, V. M., Kennedy, C. R., Rossi, S., et al. 2010, *AJ*, **139**, 1051
 R Core Team 2015, *R: A Language and Environment for Statistical Computing* (Vienna, Austria: R Foundation for Statistical Computing)
 Recio-Blanco, A., de Laverny, P., Kordopatis, G., et al. 2014, *A&A*, **567**, A5
 Roederer, I. U. 2012, *ApJ*, **756**, 36
 Roederer, I. U., Cowan, J. J., Preston, G. W., et al. 2014a, *MNRAS*, **445**, 2970
 Roederer, I. U., Lawler, J. E., Sobeck, J. S., et al. 2012, *ApJS*, **203**, 27
 Roederer, I. U., Mateo, M., Bailey, J. I., III, et al. 2016a, *AJ*, **151**, 82
 Roederer, I. U., Placco, V. M., & Beers, T. C. 2016b, *ApJL*, **824**, L19
 Roederer, I. U., Preston, G. W., Thompson, I. B., et al. 2014b, *AJ*, **147**, 136
 Roederer, I. U., Schatz, H., Lawler, J. E., et al. 2014c, *ApJ*, **791**, 32
 Rossi, S., Beers, T. C., & Sneden, C. 1999, in *ASP Conf. Ser. 165, The Third Stromlo Symp.: The Galactic Halo*, ed. B. K. Gibson, R. S. Axelrod, & M. E. Putman (San Francisco, CA: ASP), **264**
 Rossi, S., Beers, T. C., Sneden, C., et al. 2005, *AJ*, **130**, 2804
 Sakari, C. M., Placco, V. M., Hansen, T., et al. 2018, *ApJL*, **854**, L20
 Schlaufman, K. C., & Casey, A. R. 2014, *ApJ*, **797**, 13
 Schlegel, D. J., Finkbeiner, D. P., & Davis, M. 1998, *ApJ*, **500**, 525
 Shappee, B. J., Simon, J. D., Drout, M. R., et al. 2017, *Sci*, **358**, 1574
 Sharma, M., Theuns, T., & Frenk, C. 2017, arXiv:1712.05811

- Skrutskie, M. F., Cutri, R. M., Stiening, R., et al. 2006, *AJ*, **131**, 1163
- Snedden, C., Cowan, J. J., Burris, D. L., & Truran, J. W. 1998, *ApJ*, **496**, 235
- Snedden, C., Preston, G. W., McWilliam, A., & Searle, L. 1994, *ApJL*, **431**, L27
- Steinmetz, M., Zwitter, T., Siebert, A., et al. 2006, *AJ*, **132**, 1645
- Tody, D. 1986, *Proc. SPIE*, **627**, 733
- Tody, D. 1993, in ASP Conf. Ser. 52, *Astronomical Data Analysis Software and Systems II*, ed. R. J. Hanisch, R. J. V. Brissenden, & J. Barnes (San Francisco, CA: ASP), 173
- Williams, T., & Kelley, C. 2015, Gnuplot 5.0: an interactive plotting program, <http://www.gnuplot.info/>
- Wilson, E. B. 1927, *J. Am. Stat. Assoc.*, **22**, 209
- Yanny, B., Rockosi, C., Newberg, H. J., et al. 2009, *AJ*, **137**, 4377
- Yong, D., Norris, J. E., Bessell, M. S., et al. 2013, *ApJ*, **762**, 26
- Yoon, J., Beers, T. C., Placco, V. M., et al. 2016, *ApJ*, **833**, 20
- Yoon, J., Beers, T. C., Placco, V. M., & Rasmussen, K. C. 2018, *ApJ*, **833**, 20
- York, D. G., Adelman, J., Anderson, J. E., Jr., et al. 2000, *AJ*, **120**, 1579
- Zwitter, T., Siebert, A., Munari, U., et al. 2008, *AJ*, **136**, 421